Inhibition of photocorrosion and photoactivity enhancement for ZnO via specific hollow ZnO core/ZnS shell structure

Linhui Yu, Wei Chen, Danzhen Li*, Jubao Wang, Yu Shao, Miao He, Peng Wang, Xiuzhen Zheng

Research Institute of Photocatalysis, State Key Laboratory of Photocatalysis on Energy and Environment, Fuzhou University, Fuzhou 350002, PR China

ABSTRACT

Hollow ZnO core/ZnS shell structure (ZnO/ZnS HCSS) has been successfully synthesized via a microwave-assisted hydrothermal approach. It is found that such a ZnO/ZnS HCSS exhibits higher photocatalytic activity than pure ZnO and ZnS toward the liquid-phase degradation of methyl orange (MO) under UV irradiation. What is more noteworthy, it is also demonstrated that ZnO/ZnS HCSS photocatalyst overcomes the photocorrosion in comparison to pristine ZnO by mean of cycling tests toward MO. The detailed degradation process of MO over ZnO/ZnS HCSS is investigated by liquid chromatography–mass spectrometry method. And then, the roles of active species in the photocatalytic process are discussed by using different types of active species scavengers. Meanwhile, combined with the electron spin resonance and photocurrent test, the degradation mechanism of the photocatalysts is proposed. It is hoped that the work could provide valuable information on the design of specific structure materials with more excellent properties and set the foundation for the further industrial application.

© 2014 Elsevier B.V. All rights reserved.

1. Introduction

Fabrication and morphology control of materials is a crucial issue in material research. The materials with highly controlled structures and uniform morphologies may lead to novel physical and chemical properties in contract with the non-controlled, which make them enormous potential for a wide spectrum of application [1–3]. Hollow structures with thin shell layers are very attractive to achieve high surface area with a less agglomerated configuration [4], which may also offer large internal surface with special morphology to effectively capture incident illumination in combination with minimal charge transfer distance providing facile separation of photogenerated charge [5]. There are many reports where it observed that there was an enhancement of optical properties in core–shell structures with higher band gap shell materials [6]. The synthesis of core–shell functional materials and hollow spherical has attracted considerable attention in recent years as a result of the potential applications as catalyst supports, shape-selective adsorbents and the delivery system of encapsulated products for drugs, cosmetic, dye and medical [7,8].

Depending on the relative alignment of conduction band and valence band of the materials combined, semiconductor heterostructure is typically classified as type-I or type-II. In type-II situation, the lowest energy states of conduction band for electrons and valence band for holes reside on different semiconductors. This type of band location give rise to the spatial separation of electrons and holes in different regions of the heterojunction [9], which theoretically offers opportunity for the superior photocatalytic property of the heterojunction materials.

Among various materials, ZnO is close to being one of the ideal photacatalyst in several respects such as relatively inexpensive and the photogenerated holes with high oxidizing power [10]. The higher catalytic efficiencies have been reported for ZnO, and quantum efficiency of ZnO powder is also significantly larger than that of TiO_2 powder [11]. ZnS nanocrystals are also good photocatalysts because of the rapid generation of electron–hole pairs by photo-excitation and the highly negative reduction potentials of excited electrons, and it has been intensively studied because of its unique catalytic functions compared to those of TiO_2 [12]. Various photocatalysts of ZnS-modified ZnO have been attracting significant interests since their superior properties to separated ZnO and ZnS. The combination of ZnO and ZnS can yield superior material with lower photoexcitation threshold than individual components [13]. Since the bottom of the conduction band of ZnO crystal is located in the band gap of ZnS, the alignment of heterojunction can theoretically be achieved between ZnO and ZnS [14]. And the type-II band alignments result in superior optoelectronic properties of ZnO/ZnS heterostructures to their individual materials [15]. Thus

* Corresponding author. Tel.: +86 591 83779256; fax: +86 591 83779256.
  E-mail addresses: dzli@fzu.edu.cn, danzli@126.com (D. Li).

ZnO/ZnS heterostructures are deserving of effort to make them superior candidate for photocatalyst.

We have previously reported a microwave-assisted process for hollow ZnO core/ZnS shell structure [16], and the ZnO/ZnS HCSS with the special structure presents higher and superior stability of photocatalytic activity. Though many examples have been introduced to confirm the improved performances of the ZnO/ZnS heterostructures, the underlying mechanism was seldom investigated [14]. As it is well known, ZnO undergoes photocorrosion under UV light illumination [17], which is the main obstacle for ZnO to be used more widely. Herein, we subsequently investigate the photocatalytic mechanism of hollow ZnO core/ZnS shell structure with inhibited photocorrosion towards pollutant degradation. To best of our knowledge, it is the first systematic report on photocatalytic properties of hollow ZnO core/ZnS structure. And it is hoped that our work could provide valuable information on the design of specific structure materials with more excellent properties and set the foundation for the further industrial application.

2. Experimental

2.1. Materials

Zinc nitrate hexahydrate ($Zn(NO_3)_2 \cdot 6H_2O$, purchased from Aladdin Chemical Co. Ltd., Shanghai, China), thiourea (CH_4N_2S, obtained from Sinopharm Chemical Reagent Co., Ltd., Shanghai, China), dodecylamine (DDA) (supplied by Alfa Aesar China Co., Ltd., Beijing, China). All of the reagents are analytical grade and used without further purification.

2.2. Synthesis of ZnO/ZnS HCSS

The ZnO/ZnS HCSS samples were prepared using the literature method [16]. First of all, 0.185 g (1 mmol) DDA was added into 60 mL deionized water with vigorous stirring for more than 2 h. After the formation of DDA suspension, 60 mL deionized water solution with 5.95 g (20 mmol) $Zn(NO_3)_2 \cdot 6H_2O$ in it was added. Then 40 mL thiourea solution (with 30 mmol thiourea) was added into the mixture above. And then, every 20 mL of the nutrient solution as-prepared reacted at 130 °C for 15 min under microwave irradiation with CEM Discover System (Explorer48, CEM Co., and U.S.A.) operating at 150 W, 2.45 GHz. The resultant precipitate was harvested by centrifugation, then, washed with deionized water for three times and absolute ethyl alcohol once. Finally, the obtained precipitate was dried in air at ambient temperature. Moreover, to investigate the photocatalytic activity of ZnO/ZnS HCSS, pure ZnO and ZnS were prepared under the similarly experimental conditions. The synthesis of pure ZnO was performed at the reaction system analogous to that of ZnO/ZnS HCSS (reacted at 130 °C for 15 min) without thiourea. Meanwhile, pure ZnS was synthesized at 160 °C for 25 min using the same reaction mixture as that of ZnO/ZnS HCSS.

2.3. Characterization of samples

The phase constituents of the products were determined by X-ray powder diffractometer (XRD, Bruker D8 Advance with Ni-filtered Cu Kα radiation, $\lambda_\alpha = 0.15406$ nm) at 40 kV and 40 mA in the 2θ range from 25° to 70° with a scan rate of 0.02° per second. The morphologies of the obtained products were observed by ultra-high resolution scanning electron microscopy (SEM, Hitachi SU8000, operated at an accelerating voltage of 7 kV) as well as a transmission electron microscopy (TEM, FEI Tecnai G2 F20 S-TWIN, operated at an accelerating voltage of 200 kV). X-ray photoelectron spectroscopy (XPS) measurement

was performed on a Thermo Scientific ESCA Lab250 spectrometer which consists of a monochromatic Al Kα as the X-ray source, a hemispherical analyzer and sample stage with multi-axial adjustability to obtain the surface composition on the surface of the sample. All of the binding energies were calibrated by the C1s peak at 284.5 eV. Electron spin resonance (ESR) signal of the radicals spin-trapped by 5,5-dimethyl-l-pyrroline-N-oxide (DMPO) was determined on a Bruker EPR A300 spectrometer. For instance, the as-prepared sample (2.5 mg) was dispersed in 0.5 mL of purified methanol (or deionized water) into which 20 μL of DMPO/methanol (or deionized water) solution (1:10, v/v) was added. The mixture was oscillated to achieve well-blending suspension. A lamp system with filter was used as the irradiation source (λ = 254 nm). The settings for the ESR spectrometer were as follows: center field = 3512 G, microwave frequency = 9.86 GHz, and power = 6.34 mW. The photocurrent (*I–t* curves) of photocatalyst electrodes was determined by the photochemical method, which was carried out in conventional three electrode cells using a CHI600D electrochemical workstation (Shanghai Chenhua Instrument Co., Ltd., Shanghai, China). The catalyst was deposited as a film form on a 0.5 cm × 0.5 cm indium–tin–oxide conducting glass served as working electrode, the saturated calomel electrode (SCE) as the reference electrode, and Pt as the counter electrode. The electrolyte was 0.1 mol/L Na_2SO_4 aqueous solution. A lamp system with filter was used as the irradiation source (λ = 254 nm). The determination of the dyes concentration and the identification of their respective by-products were performed by a liquid chromatography–mass spectrometer (LCMS) system. An Agilent 1100 series liquid chromatogram system (Agilent Technologies, Palo Alto, CA, USA) was performed with a binary pump, 1100 UV–vis diode array detector, an auto-sample and a column thermostat. The LCMS system was equipped with a Zorbax C_{18} column (5 μm × 250 mm × 2.0 mm) and coupled on-line to Trap XCT ion-trap mass spectrometer (Agilent Technologies, CA, USA). The mass spectrometer was equipped with an electrospray ionization (ESI) source and operated in positive polarity. The ESI conditions were as follows: capillary voltage 3.5 kV; end plate offset −500 V; capillary exit 100 V; nebulizer pressure 40 psi; drying gas flow 10 L min⁻¹; temperature 350 °C. For the MO analysis, the solvents used as mobile phase were acetonitrile: 0.01 mol/L ammonium acetate (pH 6.8) = 30:70 (V/V), flow rate was 0.6 mL min⁻¹ and 20 μL of standard or sample solution were injected, and the mass range was from 50 to 400 *m/z*.

2.4. Evaluation of photocatalytic properties

The photocatalytic degradations of methyl orange (MO, 3.0×10^{-5} mol/L) aqueous solution were conducted in a quartz tube with 4.6 cm inner diameter and 17 cm length. Four UV lamps with a wavelength centered at 254 nm (Philips, TUV 4 W/G4 T5) were used as the irradiation source. A photocatalyst (40 mg) was suspended in 80 mL of MO solution and stirred for 30 min to ensure the establishment of adsorption–desorption equilibrium. An aliquot (3 mL) was taken at a certain time interval during the experiment and centrifuged (TDL-5-A) to remove the powders. The filtrates were analyzed on a Varian UV–vis spectrophotometer (Cary 50, Varian Co.). The percentage of degradation is reported as C/C_0. C is the absorption of pollutants at each irradiated time interval of the main peak of the absorption spectrum. C_0 is the absorption of the initial concentration when adsorption–desorption equilibrium was achieved. In the photocatalytic stability experiments, the catalysts were recollected by centrifugation and then re-dispersed in the same MO aqueous solution for next cycle, and other experimental parameters were same as the first testing.
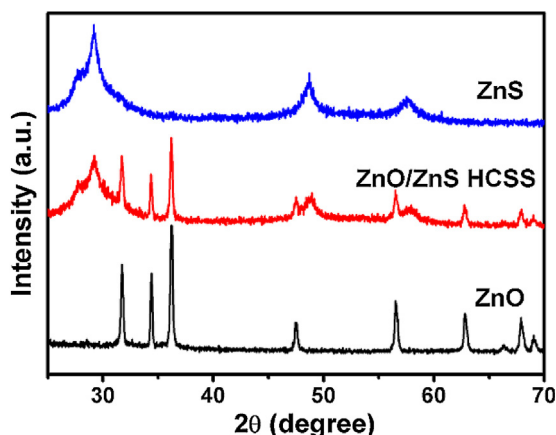
Fig. 1. XRD patterns of ZnO, ZnS and ZnO/ZnS HCSS.

3. Results and discussion

3.1. Morphology and optical properties of ZnO/ZnS HCSS

Fig. 1 shows the XRD patterns of the as-prepared ZnO, ZnS and ZnO/ZnS HCSS. The diffraction peaks of XRD patterns belong to the standard values of ZnO (JCPDS card No. 89-0511) and ZnS (JCPDS card No. 79-0043), respectively. As clearly shown in the figure, the main characteristic peaks of ZnO/ZnS HCSS contain the diffraction peaks of ZnO and ZnS. No other crystal phases can be detected in the patterns, suggesting that no impurity species were formed between ZnO and ZnS.

As shown in the SEM image (Fig. 2(a)), the formed heterostructure shows uniform peanut-like hollow structure of ZnO/ZnS HCSS composite. Besides, there exists collapsed hollow structure of ZnO/ZnS HCSS composite. The distinct contrast between the inner cavity and outer shell can be easily observed in the TEM image Fig. 2(b), which demonstrates a hollow structure. Each of the peanut-like particles has a size of 600 nm in length and 200 nm in diameter. The solid structures are composed of inner ZnO and outer ZnS, which have been verified in our previous work [16]. The rough surface may result from the aggregation of poorly crystalline or amorphous ZnS particles in the reaction process, and the loose adhesion of ZnS particles on ZnO core offers a porous structure of the ZnS shell. The HR-TEM image (Fig. 2(c)) of the solid structure further demonstrates the outer of ZnS and inter of ZnO.

To further investigate the surface compositions and chemical state of the as-prepared ZnO/ZnS HCSS, as well as the comparison with ZnO and ZnS, XPS was carried out, and the results of binding energy spectra are shown in Fig. 3. In Fig. 3(a) of O1s spectra, the ZnO/ZnS HCSS shows peak-shifting towards lower binding energy in comparison with ZnO. The S2p spectra of ZnS and ZnO/ZnS HCSS in Fig. 3(b) show no difference in the binding energy of S element, but the intensity. The Zn2p spectra are shown in Fig. 3(c) which clearly shows that ZnO/ZnS HCSS has two pairs of Zn2p fitting peaks. It indicates that there are two kinds of Zn elements in the composite, which are likely to belong to the Zn elements in ZnO and ZnS ingredients, respectively. That is, ZnO/ZnS HCSS product is composed of both ZnO and ZnS. Contrary to O1s, the Zn2p peaks of ZnO/ZnS HCSS correspond to ZnO and ZnS show shifting towards higher binding energy. In some sense, the peak-shifting of O1s in ZnO/ZnS HCSS compared with ZnO, and Zn2p of ZnO/ZnS HCSS compared with ZnO and ZnS, meaning the electron transfer between Zn and O elements, suggest the formation of heterojunction between ZnO and ZnS.

3.2. Photocatalytic activity

The photocatalytic activity of MO aqueous solution $(3.0 \times 10^{-5}$ mol/L) degradation over ZnO/ZnS HCSS, pure ZnO and ZnS were evaluated under 254 nm light irradiation. The photocatalytic degradation profiles are clearly shown in Fig. 4(b). The adsorption–desorption equilibrium of the mixture suspension is established after 30 min of stirring in dark. It clearly shows that MO solution is hardly degraded without any catalyst under 254 nm light irradiation. With the illumination time increasing, the absorption peak of MO at 464 nm decreases gradually. Only after 60 min of irradiation, it almost disappears when the mixture was ZnO/ZnS HCSS suspension, of which the absorption spectra of MO is shown in Fig. 4(a). ZnO/ZnS HCSS exhibits the best performance and about 93.7% of MO was degraded over it within 60 min, while the degradation rates over ZnS and ZnO are only 59.2% and 20.0%, respectively.

For investigating the stability of the photocatalysts, the recycled experiments for the photocatalytic degradation of MO were carried out, and the results are shown in Fig. 5. When ZnO catalyst is used for the first time, about 20.0% of MO could be degraded after 60 min of reaction as shown in Fig. 5(a). However, after three recycles, a significant decrease of the photocatalytic activity is found, and only 13.5% of MO is degraded. ZnO crystals suffer from photocorrosion and show obvious inactivation. However, ZnO/ZnS HCSS catalyst is quite stable even after three recycles of the photocatalytic degradation of MO, and above 90% of MO is degraded within 60 min, as shown in Fig. 5(b).

In order to study the photocatalytic decomposition process of MO over ZnO/ZnS HCSS, LCMS was applied to determine the residual MO and byproducts of degradation. Typical intermediates generated in the degradation process were identified from negative ionization mode mass spectra. Fig. 6 reports the chromatogram of MO solution degraded at 0, 20, 40, 60 and 80 min, respectively. The significant peaks presented at the various degradation times are labeled with the corresponding m/z values. After adsorption–desorption equilibrium in the dark, there was only one strong peak in the chromatogram appeared at 3.1 min, which belongs to MO molecule. However, after 20 min of UV light irradiation, another peak appears at 2.6 min belonging to degradation byproduct is also observed in the chromatogram. With the irradiation time increasing, the peaks of residual MO gradually disappears, but the intensity of the byproduct peak slightly increases, indicating most of dye are removed from the solution and some of them are transformed to other small molecule products.

The proposed fragmentation scheme is the unavoidable presence of odd electrons species. However, the structure of MO molecule does not allow easy formation of neutral fragments if one excludes SO_2 or SO_3 molecules. Homolytic bond breaking becomes thus competitive in spite of the absence of any stabilization of the odd electrons by the conjugated π electron system due to the difference in the orbital symmetry [18]. After this preliminary characterization of the fragmentation behavior during the degradation, the constituents of the fragments for different reaction times were analyzed. In Fig. 6, there are also the corresponding mass spectra of the degradation byproducts of MO. And the significant mass peaks are also labeled with the corresponding m/z values. As clearly visible in the figure, two weak mass peaks of the byproducts (m/z = 217, 290, 375) can be observed. The m/z values mentioned above might have some deviation from the molecular weight because of the hydrogen losing.

For both of the dyes and byproducts, the corresponding mass peak intensities vary gradually with the increase of irradiation time. The changes of mass spectrum intensity of the main peaks corresponding view are shown in Fig. 7. It shows that the intensity of the peak (m/z = 304) for MO was initially 9.8×10^5 counts. And after
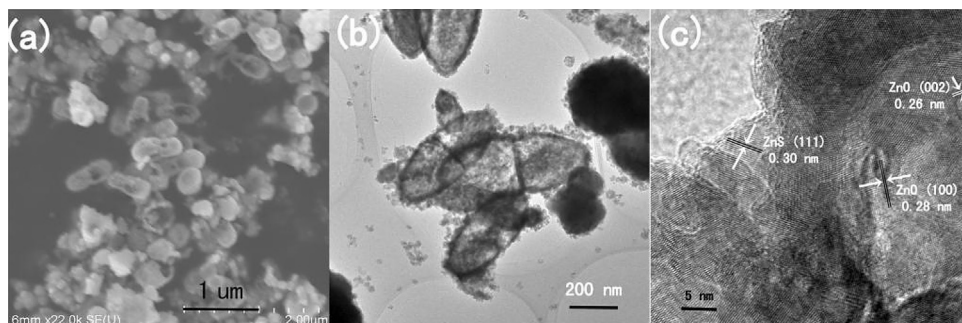
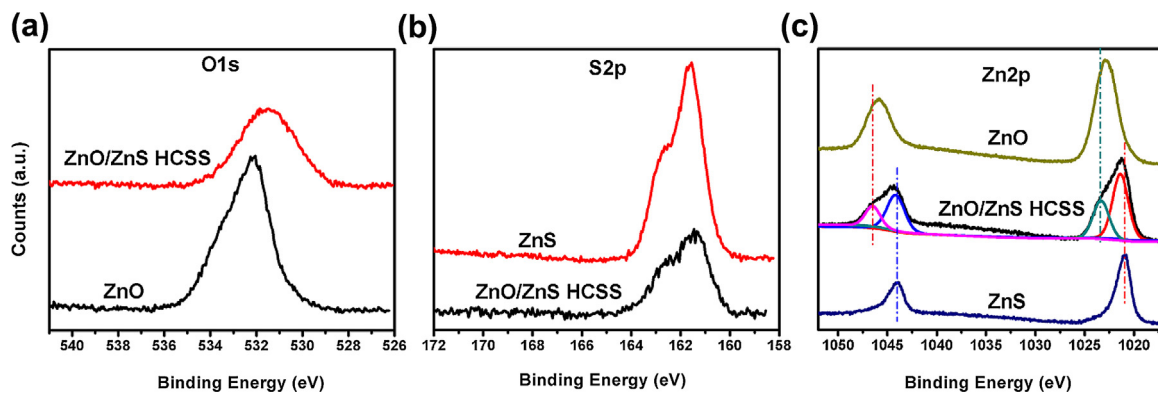**Fig. 2.** SEM (a), TEM (b) and HR-TEM (c) of ZnO/ZnS HCSS.

Fig. 3. XPS spectra of ZnO, ZnS and ZnO/ZnS HCSS: (a) O1s, (b) S2p, (c) Zn2p.
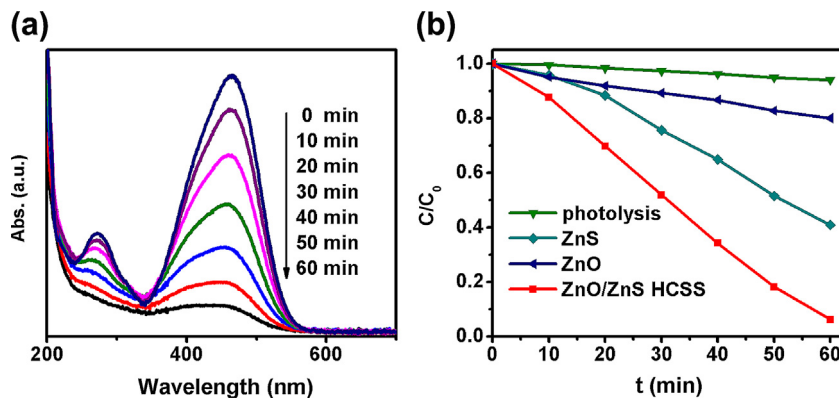

Fig. 4. (a) Absorption spectra of MO in the presence of ZnO/ZnS HCSS under exposure to UV light, (b) photocatalytic degradation of MO over ZnO/ZnS HCSS, ZnO and ZnS under 254 nm irradiation.
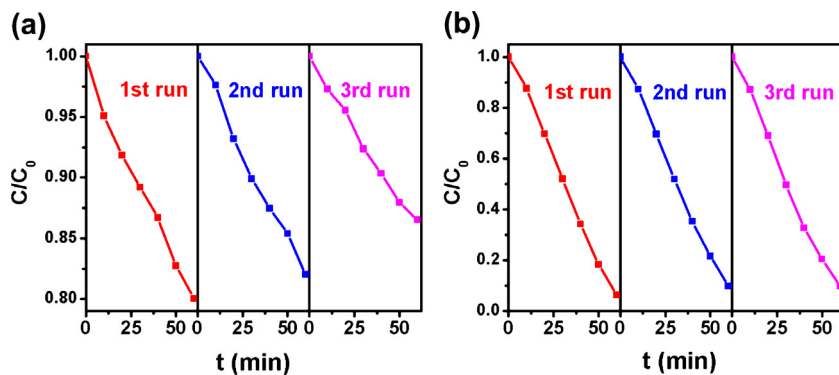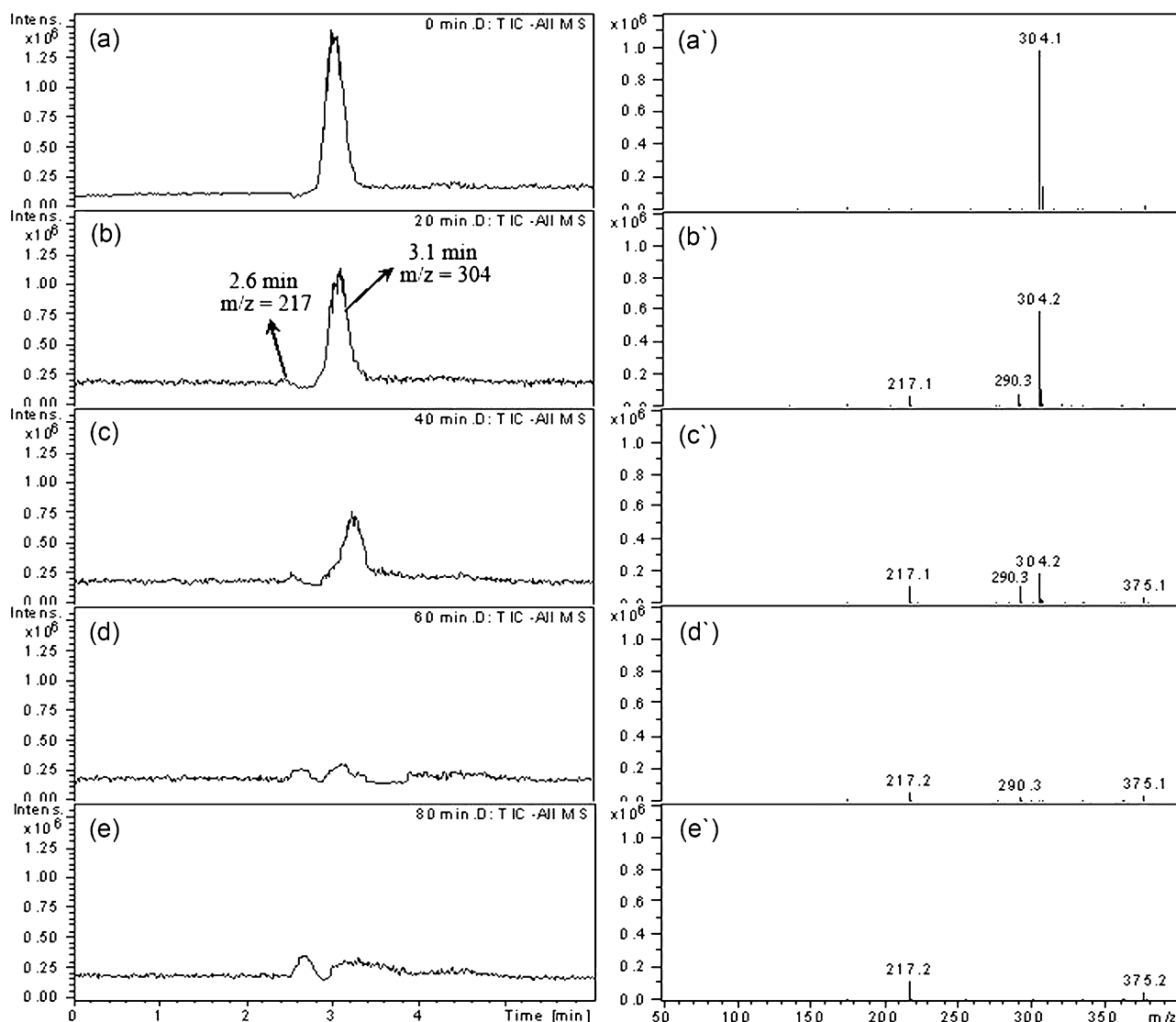

Fig. 5. Degradation of MO over ZnO (a) and ZnO/ZnS HCSS (b) under 254 nm light irradiation in three successive cycles.

Fig. 6. LCMS chromatograms of degraded MO solutions at different irradiation intervals. (a)–(e) Chromatograms of MO solution after 0, 20, 40, 60 and 80 min of irradiation, respectively. (a′)–(e′) Corresponding mass spectrum view of the main byproducts.

80 min of irradiation, it almost reduces to zero. For the degradation byproducts (m/z = 217, 290), the peak intensities firstly increase and then decrease, indicating both these byproducts are unstable and will finally be degraded in a large degree when the reaction time increases. It was worth noticing that there is a byproduct having an m/z value of 375 higher than that of the parent molecule. We have inferred its structure, whose molecular weight is in accord with the hypothesis of the formation of carboxyl groups. In the reaction process, two of the methyl groups (–CH$_3$) bonded to nitrogen atom in MO molecule are oxidized to carboxyl groups (–COOH). Furthermore, its intensity increases in the initial 40 min of irradiation. But in the following 40 min, it rises and falls around 4.0×10^4 counts, indicating this fragment is very stable and difficult to degrade.

On the basis of above LCMS analysis and the structure of MO molecule, we have inferred the possible structures of degradation byproducts and the pathways of photocatalytic degradation as shown in Scheme 1. It is necessary to point out that the inferred degradation fragments may have some isomeric compounds for the complexity of MO molecule. Compared with the degradation pathway of MO over other photocatalysts [19–28], the uniqueness shows in the carboxylation and hydroxylation process, which is

ascribe to the stronger oxidizability of the composite on account of the lower location of the valence band (VB).

3.3. Comparisons of photocatalytic mechanism

It is important to detect the main oxidative species in the photocatalytic process for revealing the photocatalytic mechanism. Therefore, different types of active species scavengers are added in catalyst system. Fig. 8 shows MO degradation curves over ZnO/ZnS HCSS under conditions such as air-equilibrated, N$_2$-bubbled, O$_2$-bubbled, adding benzoquinone (BQ), adding CH$_3$OH, and adding tert-butyl alcohol (t-BA), respectively. The BQ is an effective active species scavenger for O$_2^{\bullet-}$ by a simple electron transfer mechanism [29]. As shown in the figure, the addition of BQ (1 mg) provokes a large degree of inhibition of the MO degradation, which confirms the indispensable role of O$_2^{\bullet-}$ in the degradation process. To further verify the decisive role of O$_2^{\bullet-}$, experiments with conditions of air-equilibrated, N$_2$-bubbled and O$_2$-bubbled were carried out. Dissolved O$_2$ as an electron scavenger to produce a variety of active oxygen species [30], such as O$_2^{\bullet-}$, promotes the degradation process significantly. When it is bubbled into the reaction system at
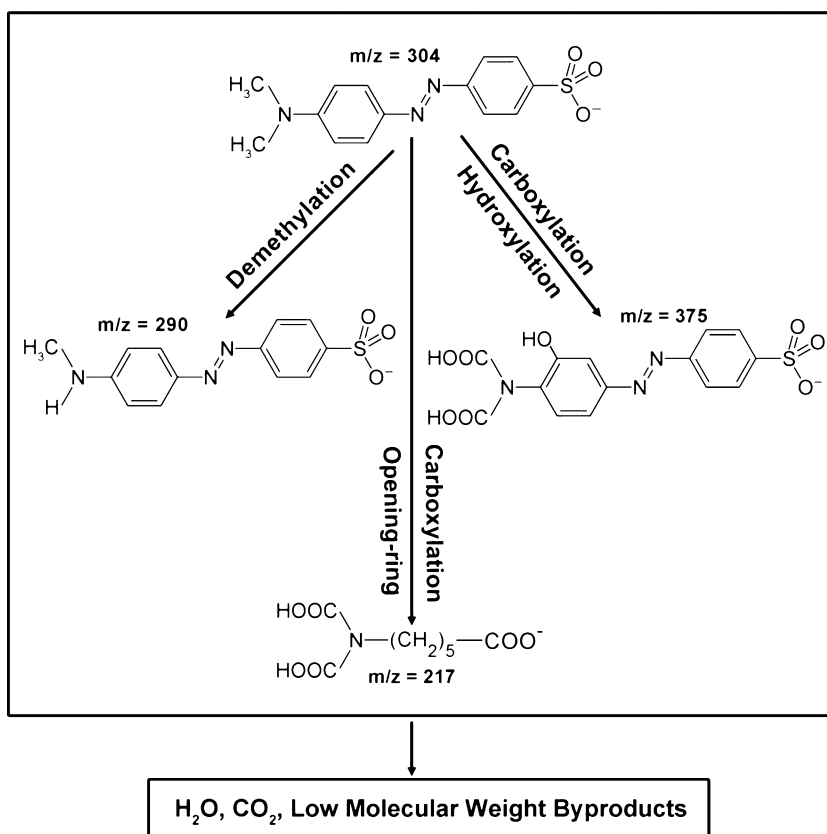
Scheme 1. Proposed degradation pathways for MO photocatalytic degradation over ZnO/ZnS HCSS photocatalysts.

the flow rate of 20 mL min^{-1}, the degradation tendency and ratio of MO solution seem to be similar with the air-equilibrated condition, and about 90.2% of MO is degraded within 60 min. In addition, N_2 was bubbled into the suspension at the rate of 20 mL min^{-1} to ensure that the reaction was operated without O_2. As clearly shown, the degradation rate is obviously slow and only about 21.6% of MO is degraded within 60 min of reaction. The results undoubtedly demonstrate the important role of $O_2^{\bullet-}$ evolved by dissolved O_2 in the reaction system. And the hardly changed degradation rate of MO under the condition with bubbled O_2 may be due to the sufficient dissolved O_2 in the reaction system. Furthermore, the addition of a scavenger of $^\bullet$OH radicals (1 mmol t-BA) [22] only causes a small change in the photodegradation of MO. Thus, the MO oxidation is driven by the contribution of $^\bullet$OH radicals to a lesser

extent. On the contrary, the photocatalytic activity of ZnO/ZnS HCSS could be greatly suppressed by the addition of a scavenger for holes [31] (1 mmol CH_3OH). This result suggests that the photogenerated holes are one of the main oxidative species in MO degradation system over ZnO/ZnS HCSS. It is concluded that the importance of the roles follows the order: $O_2^{\bullet-} > h^+ > {}^\bullet OH$, which is similar to the pure ZnO and ZnS (Fig. S1).

Through the comparison, we can conclude that the degradation of MO solution over ZnO/ZnS HCSS photocatalyst is driven mainly by the participation of $O_2^{\bullet-}$ radicals and holes, and to a lesser extent by the contribution of $^\bullet$OH radicals.
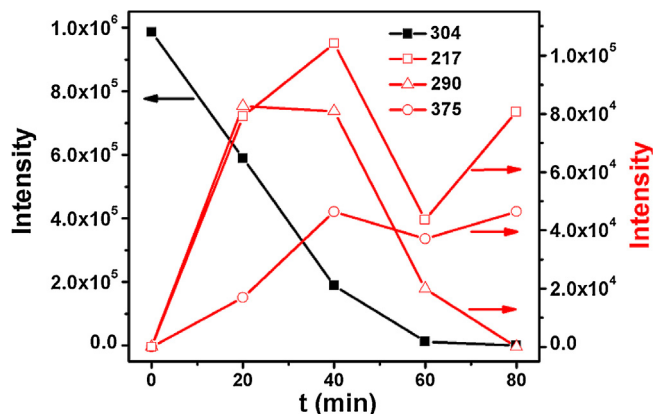
**Fig. 7.** Mass spectra view changes of the peak intensity appeared in photocatalytic process of MO solution.
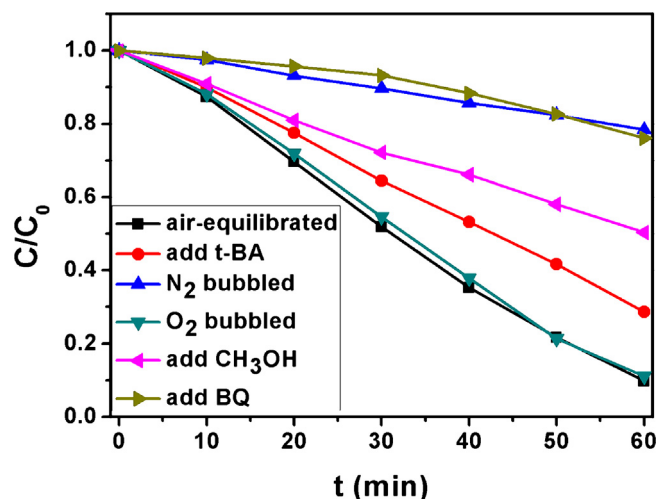
Fig. 8. Photocatalytic degradation of MO over ZnO/ZnS HCSS under different conditons exposure to irradiation of 254 nm.
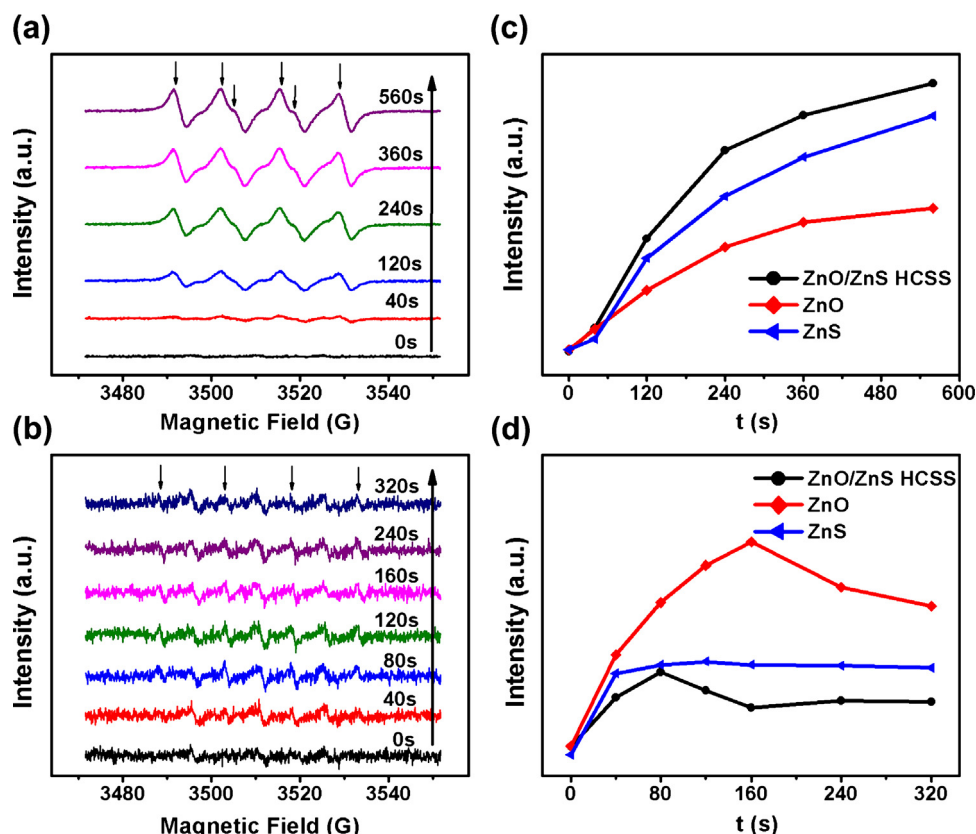
Fig. 9. DMPO spin-trapping ESR spectra of DMPO-$O_2{}^{\bullet-}$ (a) and DMPO-$^{\bullet}$OH (b) in ZnO/ZnS HCSS with different irradiation time, and the signals of DMPO-$O_2{}^{\bullet-}$ (c) and DMPO-$^{\bullet}$OH (d) of ZnO/ZnS HCSS, ZnO, ZnS with the increasing of irradiation time.

ESR with DMPO technique was also used to detect the active species ($O_2{}^{\bullet-}$ and $^{\bullet}$OH) [32] and the changes of their quantities in the photocatalytic reaction system of ZnO/ZnS HCSS. ESR signals of $O_2{}^{\bullet-}$ and $^{\bullet}$OH species for all the representative products were detected at the same condition, and the results are shown in Fig. 9. The signal of DMPO-$O_2{}^{\bullet-}$ can be achieved in methanolic dispersions of the catalysts under 254 nm light irradiation. The patterns of the signals for ZnO/ZnS HCSS are shown in Fig. 9(a). Herein, the strong signals of DMPO-$O_2{}^{\bullet-}$ species reveal the transfer pathway of electrons and demonstrate the important effect of dissolved O_2. In Fig. 9(c), the curves display the change tendency of the signals of DMPO-$O_2{}^{\bullet-}$ species upon the irradiation time for all the products.

All of the signals show rising tendency during the irradiation period. In addition, there is a regularity for the signal intensities among the three products, with ZnO/ZnS HCSS > ZnS > ZnO. It is consistent with the results of photocatalytic activities and further demonstrates the important roles of $O_2{}^{\bullet-}$ species in the photocatalytic degradation reaction. In Fig. 9(b), the ESR signal for ZnO/ZnS HCSS belonging to DMPO-$^{\bullet}$OH is detected in aqueous dispersions of the catalyst. All the four main characteristic peaks (labeled by the arrows) are very weak, suggesting there is few $^{\bullet}$OH species in the aqueous dispersions of the catalyst. The signals of DMPO-$^{\bullet}$OH for other two products are very weak either. The change tendency of the signals of DMPO-$^{\bullet}$OH species for all the products was also detected. During the irradiation period, the signal intensities for the three products show opposite regularity compared to that of DMPO-$O_2{}^{\bullet-}$ species, with ZnO > ZnS > ZnO/ZnS HCSS. In addition, the signal intensity for ZnO significantly decreases as the irradiation time increases, which confirms the inactive phenomenon of ZnO photocatalyst. The weak signals of DMPO-$^{\bullet}$OH suggest that the hydroxyl radicals are the extraessential active species in the photocatalytic reaction system of ZnO/ZnS HCSS.
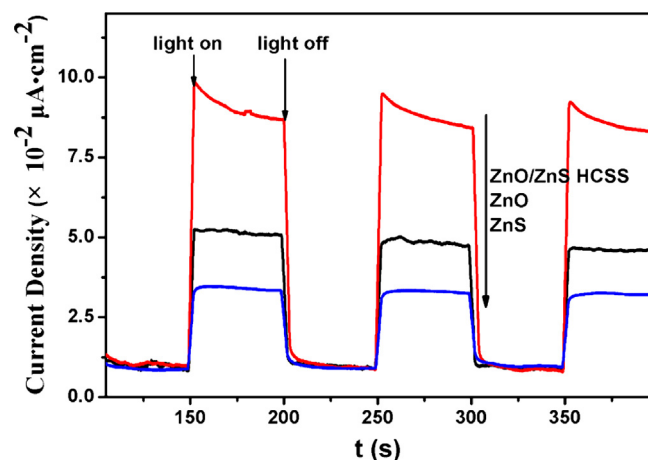
Fig. 10. Transient photocurrent response of ZnO/ZnS HCSS, ZnO and ZnS under irradiation of 254 nm.

Photoelectrochemical experiments were performed to investigate the electronic interaction between ZnO and ZnS. It is clear shown in Fig. 10 that fast and uniform photocurrent responses are detected for each switch-on and switch-off event in all of the electrodes and the photo-responsive phenomenon is entirely reversible. With 254 nm UV light irradiation, the photocurrent of the ZnO/ZnS HCSS electrode is about 1.8 times as high as that of the pure ZnO electrode and about 3 times as high as that of pure ZnS electrode. Under visible light irradiation, ZnO shows almost no photocurrent response. The photocurrent enhancement of ZnO/ZnS HCSS photocatalyst indicates an enhanced separation efficiency of photogenerated electrons and holes, which could be attributed
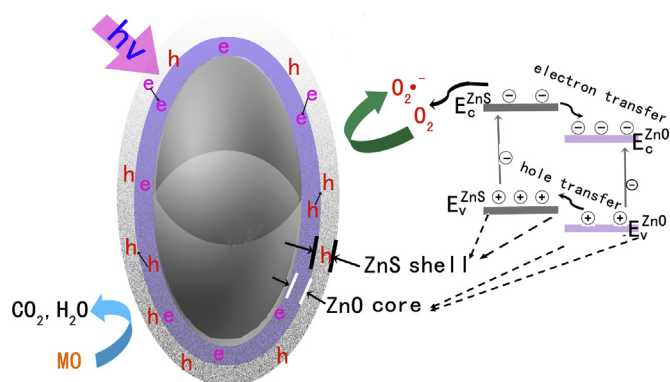
Scheme 2. Proposed mechanism for degradation of MO over ZnO/ZnS HCSS under UV light irradiation.

to the interaction of ZnO and ZnS ingredients in ZnO/ZnS HCSS. Once more, this confirms why ZnO/ZnS HCSS composite has more excellent photocatalytic properties than pure ZnO and ZnS photocatalysts.

Thus far, we have discussed in detail the optimized photocatalytic activity and stability for ZnO/ZnS HCSS, as well as the mechanism of the photocatalytic degradation. The superior photocatalytic activity and stability owe to the distinctively hollow core/shell morphology and porous ZnS shell, which offer a favorable structure for reactants exchanging between inner and outer of the ZnO/ZnS HCSS. On the other hand, the sufficient contact and reciprocates between the two ingredients are the crucial factors in forming effective separation and transfer of electrons and holes. The proposed degradation mechanism of MO over ZnO/ZnS HCSS and the relationship of band structure between ZnO and ZnS are schematically presented in Scheme 2. The heterojunction is formed after deposition of ZnS on the surface of ZnO, which changes the charge transfer process [33]. Since the bottom of the conduction band of ZnO crystal is located between the band edges of ZnS, the band alignment can theoretically be achieved between ZnO and ZnS [14]. And the core/shell structure of ZnO/ZnS HCSS composites offers a built-in electric field what provides a driving force for charge carriers transition. Detailedly speaking, the conduction band of ZnS lies at a more negative potential (vs NHE) than that of ZnO, while the valence band of ZnO is more positive than that of ZnS [34]. Thereby, the photoexcited electrons deviate from the photogenerated holes in the valence band of ZnO core and ZnS shell to the conduction band. Because of the negative potential of ZnS conduction band, the electrons then impregnated into that of ZnO core. Meanwhile, the photagenerated holes transfer from the valence band of ZnO core to that of ZnS shell. In addition, the attack of the surface oxygen atom by the holes transported to the solid-solution interface results in the escape of oxygen from the surface, which the photocorrosion come into being [35]. While the effective transfer of holes from ZnO core to ZnS shell opportunely prevent them from attacking the surface oxygen of ZnO and suppress the photocorrosion effect. And the coverage of the ZnS shell protects the surface oxygen of ZnO from exposure to solution as well localise them. The simultaneous transfer of electrons and holes in the ZnO/ZnS HCSS system yield higher separation efficiency of electron–hole pairs, which is demonstrated by the transient photocurrent shown in Fig. 10, and the process prolongs the lifetime of the charge carriers as well. And those both benefit the superior photocatalytic activity and stability of ZnO/ZnS HCSS to that of individual ZnO and ZnS. The porous ZnS shell provides transfer channel for O_2, and the absorbed O_2 on the surface may capture the transferred electron on the conduction band of ZnS and ZnO, then forms the active species $O_2^{\bullet-}$. The generated $O_2^{\bullet-}$ species, the transfered holes on

the surface and bits of $^{\bullet}$OH species, even some e_{aq}^- or $^{\bullet}$H species are likely to be formed in the photocatalytic process, and then attack the adsorbed MO molecules and degraded them into the intermediates with small molecules, even carbon dioxide and water. Thus, the photocatalysis efficiency is significantly enhanced and the possible photodegradation process can be proposed as follows [36,37]:

$$(1) ZnO + h\upsilon \to ZnO(e^- + h^+)$$

$$(2) ZnS + h\upsilon \to ZnS(e^- + h^+)$$

$$(3) h^+ + H_2O \to {}^{\bullet}OH + H^+$$

$$(4) e^- + O_2 \to O_2^{\bullet-}$$

$$(5) O_2^{\bullet-} + 2H^+ + e^- \to H_2O_2$$

$$(6) H_2O_2 + e^- \to {}^{\bullet}OH + OH^-$$

$$(7) O_2^{\bullet-}(h^+, H_2O_2, {}^{\bullet}OH) + MOdye \to Degraded products$$

4. Conclusions

Hollow ZnO core/ZnS shell structure has been prepared via a microwave-assisted hydrothermal method and exhibits superior photocatalytic performance to separated ZnO or ZnS under UV irradiation. Meanwhile, a series of proposed intermediate products are explored by LCMS. The $O_2^{\bullet-}$ species and hole play the most important role in the photocatalytic degradation process, and to a lesser extent by the contribution of $^{\bullet}$OH radicals. At last, the photocatalytic degradation mechanism over ZnO/ZnS HCSS has been detailedly discussed.

Acknowledgment

Appendix A. Supplementary data

Supplementary data associated with this article can be found, in the online version, at http://dx.doi.org/10.1016/j.apcatb.2014.09.055.

References

[1] Z. Yang, Y. Lu, Z. Yang, Chem. Commun. 0 (2009) 2270–2277.
[2] J. Pang, L. Yang, D.A. Loy, H. Peng, H.S. Ashbaugh, J. Mague, C.J. Brinker, Y. Lu, Chem. Commun. 0 (2006) 1545–1547.
[3] Y. Zhu, T. Mei, Y. Wang, Y. Qian, J. Mater. Chem. 21 (2011) 11457–11463.
[4] J.-H. Lee, Sens. Actuat. B: Chem. 140 (2009) 319–336.
[5] Z. Wang, J. Hou, C. Yang, S. Jiao, K. Huang, H. Zhu, Energy Environ. Sci. 6 (2013) 2134–2144.
[6] S.K. Panda, A. Dev, S. Chaudhuri, J. Phys. Chem. C 111 (2007) 5039–5043.
[7] X. Ding, K. Yu, Y. Jiang, B. Hari, H. Zhang, Z. Wang, Mater. Lett. 58 (2004) 3618–3621.
[8] X. Guo, X. Liu, B. Xu, T. Dou, Colloids Surf. A: Physicochem. Eng. Aspects 345 (2009) 141–146.
[9] U. Soni, A. Pal, S. Singh, M. Mittal, S. Yadav, R. Elangovan, S. Sapra, ACS Nano 8 (2014) 113–123.
[10] C. Hariharan, Appl. Catal. A: Gen. 304 (2006) 55–61.
[11] S. Chakrabarti, B.K. Dutta, J. Hazard. Mater. 112 (2004) 269–278.
[12] J.-S. Hu, L.-L. Ren, Y.-G. Guo, H.-P. Liang, A.-M. Cao, L.-J. Wan, C.-L. Bai, Angew. Chem. Int. Ed. 44 (2005) 1269–1273.
[13] J. Lahiri, M. Batzill, J. Phys. Chem. C 112 (2008) 4304–4307.
[14] D. Wu, Y. Jiang, Y. Yuan, J. Wu, K. Jiang, J. Nanopart. Res. 13 (2011) 2875–2886.
[15] D.Y. Wang, I.S. Wang, I.S. Huang, Y.C. Yeh, S.S. Li, K.H. Tu, C.C. Chen, C.W. Chen, J. Phys. Chem. C 116 (2012) 10181–10185.

[16] W. Chen, H. Ruan, Y. Hu, D. Li, Z. Chen, J. Xian, J. Chen, X. Fu, Y. Shao, Y. Zheng, CrystEngComm 14 (2012) 6295–6305.

[17] R.T. Sapkal, S.S. Shinde, T.R. Waghmode, S.P. Govindwar, K.Y. Rajpure, C.H. Bhosale, J. Photochem. Photobiol. B: Biol. 110 (2012) 15–21.

[18] C. Baiocchi, M.C. Brussino, E. Pramauro, A.B. Prevot, L. Palmisano, G. Marcı, Int. J. Mass Spectrom. 214 (2002) 247–256.

[19] Z. Chen, D. Li, W. Zhang, Y. Shao, T. Chen, M. Sun, X. Fu, J. Phys. Chem. C 113 (2009) 4433–4440.

[20] Y. He, D. Li, G. Xiao, W. Chen, Y. Chen, M. Sun, H. Huang, X. Fu, J. Phys. Chem. C 113 (2009) 5254–5262.

[21] W. Li, D. Li, Z. Chen, H. Huang, M. Sun, Y. He, X. Fu, J. Phys. Chem. C 112 (2008) 14943–14947.

[22] C. Li, D. Jiang, L. Zhang, J. Xia, Q. Li, Langmuir (2012), 120607165527003.

[23] W. Li, D. Li, J. Xian, W. Chen, Y. Hu, Y. Shao, X. Fu, J. Phys. Chem. C 114 (2010) 21482–21492.

[24] W. Li, D. Li, W. Zhang, Y. Hu, Y. He, X. Fu, J. Phys. Chem. C 114 (2010) 2154–2159.

[25] M. Sun, D. Li, Y. Chen, W. Chen, W. Li, Y. He, X. Fu, J. Phys. Chem. C 113 (2009) 13825–13831.

[26] M. Sun, D. Li, W. Li, Y. Chen, Z. Chen, Y. He, X. Fu, J. Phys. Chem. C 112 (2008) 18076–18081.

[27] W. Zhang, D. Li, Z. Chen, M. Sun, W. Li, Q. Lin, X. Fu, Mater. Res. Bull. 46 (2011) 975–982.

[28] W. Zhang, D. Li, M. Sun, Y. Shao, Z. Chen, G. Xiao, X. Fu, J. Solid State Chem. 183 (2010) 2466–2474.

[29] R. Palominos, J. Freer, M.A. Mondaca, H.D. Mansilla, J. Photochem. Photobiol. A: Chem. 193 (2008) 139–145.

[30] Y. Lin, D. Li, J. Hu, G. Xiao, J. Wang, W. Li, X. Fu, J. Phys. Chem. C 116 (2012) 5764–5772.

[31] T. Puangpetch, S. Chavadej, T. Sreethawong, Energy Convers. Manage. 52 (2011) 2256–2261.

[32] Z. Wang, W. Ma, C. Chen, H. Ji, J. Zhao, Chem. Eng. J. 170 (2011) 353–362.

[33] H.X. Sang, X.T. Wang, C.C. Fan, F. Wang, Int. J. Hydrogen Energy 37 (2012) 1348–1355.

[34] Y. Hu, H. Qian, Y. Liu, G. Du, F. Zhang, L. Wang, X. Hu, CrystEngComm 13 (2011) 3438–3443.

[35] H. Fu, T. Xu, S. Zhu, Y. Zhu, Environ. Sci. Technol. 42 (2008) 8064–8069.

[36] D. Lin, H. Wu, R. Zhang, W. Zhang, W. Pan, J. Am. Ceram. Soc. 93 (2010) 3384–3389.

[37] Y. Linhui, R. Hong, Z. Yi, L. Danzhen, Nanotechnology 24 (2013) 375601.